


## Helicity maximization below the diffraction limit

Mina Hanifeh<sup>1</sup>,\* Mohammad Albooyeh, and Filippo Capolino<sup>1</sup>,\*

*Department of Electrical Engineering and Computer Science, University of California, Irvine, Irvine, California 92697, USA*

 (Received 3 October 2018; revised 29 July 2020; accepted 9 September 2020; published 26 October 2020)

Optimally chiral electromagnetic fields with maximized helicity density, recently introduced by Hanifeh *et al.* [M. Hanifeh, M. Albooyeh, and F. Capolino, *ACS Photonics* **7**, 2682 (2020)], enable chirality characterization of optically small nanoparticles. Here we demonstrate a technique to obtain optimally chiral near fields that leads to the maximization of helicity density under the constraint of constant energy density, beyond the diffraction limit. We show how optimally chiral illumination induces balanced electric and magnetic dipole moments in an achiral dielectric nanoantenna, which leads to generating optimally chiral scattered and total near fields. In particular, we explore helicity and energy densities in the near field of a spherical dielectric nanoantenna illuminated by an optimally chiral combination of azimuthally and radially polarized beams. This beam combination generates parallel induced electric and magnetic dipole moments in the nanoantenna that in turn generate an optimally chiral scattered field with the same helicity sign of the incident field. The application of helicity maximization to near fields results in helicity enhancement at the nanoscale, which is of great advantage in the detection of nanoscale chiral samples, microscopy, and optical manipulation of chiral nanoparticles.

DOI: [10.1103/PhysRevB.102.165419](https://doi.org/10.1103/PhysRevB.102.165419)

### I. INTRODUCTION

Chiral nanoparticles are not superimposed on their mirror images [1], and each pair of their mirror-imaged structures, called enantiomers, have the same constitutions but different *optical* properties [2]. Considering their broad range of applications in sciences and technologies in areas like chemistry, biology, and pharmacology [3–5], many studies have been performed to enhance the range of chirality detection, e.g., by introducing the concept of super-chiral light [6], by the use of near fields of plasmonic structures [7–25], of dielectric structures [26–31], and structures combining the two [32,33].

Recently, in Ref. [34], we have introduced the concept of helicity maximization and have defined optimally chiral fields that possess the maximum helicity density among all possible fields with same energy density. In optimally chiral fields the electric  $\mathbf{E}$  and magnetic  $\mathbf{H}$  field components (in phasor terms) satisfy the condition

$$\mathbf{E} = \pm i\eta_0\mathbf{H}, \quad (1)$$

where the  $+/-$  sign indicates positive/negative helicity density and  $\eta_0$  is the intrinsic wave impedance of vacuum. Monochromatic electromagnetic fields with time dependence  $\exp(-i\omega t)$ , where  $\omega$  is the angular frequency, are considered throughout the paper.

In optimally chiral fields, i.e., fields satisfying Eq. (1), the linear relationship  $|h| = u/\omega$  exists between time-averaged helicity density, defined as  $h = \Im\{\mathbf{E} \cdot \mathbf{H}^*\}/(2\omega c_0)$ , and time-averaged energy density,  $u = (\epsilon|\mathbf{E}|^2 + \mu_0|\mathbf{H}|^2)/4$ , of the field. Here “ $*$ ” denotes complex conjugation and  $\Im\{\cdot\}$  indicates the imaginary part of a complex value. Moreover,  $\epsilon_0$ ,  $\mu_0$ ,

and  $c_0$  are, respectively, the permittivity, permeability, and speed of light in vacuum. The concept of helicity density of electromagnetic fields is discussed also in Refs. [35–41]. In Ref. [34], we have elaborated that it is possible to characterize the chirality of a nanoparticle when fields with maximum helicity density, called optimally chiral fields, are employed in the determination of the dissymmetry factor  $g$  [42], defined as

$$g = \frac{\Delta P_{\text{ext}}}{\bar{P}_{\text{ext}}}. \quad (2)$$

Here,  $\bar{P}_{\text{ext}}$  and  $\Delta P_{\text{ext}}$  are, respectively, the arithmetic average of and difference between the two extinction powers of the nanoparticle sample, measured in the two experiments where optimally chiral fields with  $\mathbf{E} = +i\eta_0\mathbf{H}$  and  $\mathbf{E} = -i\eta_0\mathbf{H}$  are used. The dissymmetry factor  $g$  is proportional to the ratio of helicity over energy density of the excitations [6,34,43]. Conveniently, the use of optimally chiral fields enables the removal of the values of helicity and energy densities of the field from the expression of the dissymmetry factor  $g$  due to the linear relationship  $|h| = u/\omega$ . This offers a simplified way for chirality characterization at nanoscale, as shown in Ref. [34].

Here we investigate how to generate optimally chiral near-field and helicity enhancement at nanoscale by employing an achiral dielectric nanoantenna (NA). To that end, we show that helicity density of the near field of a NA is divided into three parts: helicity densities of the *incident* and *scattered* fields and a part related to *interference* between these two. We prove that to have an optimally chiral *total* near field (the superposition of incident and scattered fields) it is required to excite the NA by an optimally chiral incident field. We also derive the required conditions a NA needs to satisfy in terms of induced electric and magnetic dipole moments, and hence of its dipolar polarizabilities, to generate an optimally chiral scattered near

\*mhanifeh@uci.edu; f.capolino@uci.edu

field whose helicity is constructive with that of the incident field and the “interference” helicity term.

One example of an optimally chiral field to excite the NA is a plane wave with circular polarization. Helicity density around a dielectric NA exposed to circularly polarized light has been studied in Refs. [26–30]. In particular, in Ref. [27] we have shown that the near field of an array of spherical dielectric NAs illuminated by a plane wave with circular polarization is very close to being optimally chiral. Other practical examples of optimally chiral fields can be obtained using structured light. In this paper we show that the superposition of an azimuthally polarized beam (APB) [44–49] and a radially polarized beam (RPB) [49–57], called ARPB, with appropriate relative amplitudes and phase difference [58] is optimally chiral. In particular, we investigate the helicity density of an optimally chiral ARPB and how this can be used to excite a NA made of a high-refractive-index dielectric material, e.g., by silicon (Si) or titanium dioxide (TiO<sub>2</sub>). Note that an achiral NA made of a high index material can also represent the tip of a scanning probe microscope; therefore this work has also several potential applications in nanoscale chiral studies [58].

We investigate the helicity density of the near field of a spherical dielectric NA illuminated by an optimally chiral ARPB. This analysis reveals that the interference helicity density has a considerable role in helicity enhancement of the near field of the NA, which emphasizes the importance of excitation to be optimally chiral. Moreover, in the present analysis we elaborate that maximum helicity enhancement does not coincide with maximum energy enhancement for optically small NAs modeled by induced dipole moments. Indeed, we show that the radius of a dielectric NA, which results in generating maximum helicity enhancement, takes a value between those radii corresponding to maximum energy density enhancement and an optimally chiral near field. A related concept involving the ARPB was also considered in [59] to excite a NA with both electric and magnetic dipole moments; however, in that work the two RPB and APB beams were in phase so the composed beam does not provide chiral light, while in this paper the ARPB carries *optimally* chiral light. In [59] helicity of the *scattered* field was generated by having a proper phase shift between the electric and magnetic polarizabilities of the NA; however, the *incident* field was not chiral, and the concept of interference helicity was not considered.

Here we focus on generating optimally chiral electromagnetic fields, reaching the upper bound of helicity density at a given energy density introduced in Ref. [34]. Potential applications are in chiral force microscopy at nanoscale [58,60] and circular dichroism at nanoscale [6,27,34,43,61]. Interested readers are referred to Refs. [35,36,41,62–65] for stimulating discussions about conservation of helicity.

## II. OPTIMALLY CHIRAL NEAR FIELD

Near fields of NAs overcome the diffraction limit and provide high spatial resolution in microscopy and spectroscopy. In the quest for chiral spectroscopy and microscopy at nanoscale, we found it essential to investigate how to design a NA that generates maximized helicity density, with spatial

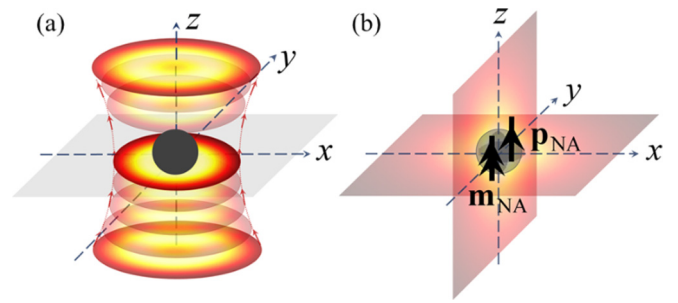


FIG. 1. Near field of a NA is used to generate enhanced helicity density with respect to that of an incident beam. (a) An optical beam propagating along the  $+z$  direction illuminates a NA located at the center of the coordinate system. (b) The dielectric NA is modeled by induced electric and magnetic dipole moments  $\mathbf{p}_{\text{NA}}$  and  $\mathbf{m}_{\text{NA}}$ , respectively, and their scattered near fields demonstrate high helicity density in the vicinity of the NA.

focusing below the diffraction limit. To that end we assume that a NA is located at the center of a Cartesian coordinate system and is illuminated by an optical beam propagating along the  $+z$  direction, as in Fig. 1(a).

The *total* near field of a NA includes contributions from both the incident optical beam and its scattered near field, denoted respectively by subscripts “inc” and “sca”:

$$\begin{aligned}\mathbf{E} &= \mathbf{E}_{\text{sca}} + \mathbf{E}_{\text{inc}}, \\ \mathbf{H} &= \mathbf{H}_{\text{sca}} + \mathbf{H}_{\text{inc}}.\end{aligned}\quad (3)$$

Substituting Eq. (3) into  $h = \Im\{\mathbf{E} \cdot \mathbf{H}^*\}/(2\omega c_0)$ , the helicity density  $h$  of the near field around a NA reads

$$h = h_{\text{inc}} + h_{\text{sca}} + h_{\text{int}}, \quad (4)$$

where  $h_{\text{sca}} = \Im\{\mathbf{E}_{\text{sca}} \cdot \mathbf{H}_{\text{sca}}^*\}/(2\omega c_0)$  and  $h_{\text{inc}} = \Im\{\mathbf{E}_{\text{inc}} \cdot \mathbf{H}_{\text{inc}}^*\}/(2\omega c_0)$  are, respectively, the helicity densities of the scattered and incident fields. Moreover,  $h_{\text{int}}$ , which we call *interference helicity density*, reads

$$h_{\text{int}} = \frac{1}{2\omega c_0} \Im\{\mathbf{E}_{\text{sca}} \cdot \mathbf{H}_{\text{inc}}^* + \mathbf{E}_{\text{inc}} \cdot \mathbf{H}_{\text{sca}}^*\}. \quad (5)$$

Equation (4) suggests that for an improvement of helicity density we need to boost some of the helicity densities  $h_{\text{sca}}$  and  $h_{\text{int}}$ . Moreover, we need to manipulate incident and scattered fields so that all terms in Eq. (4) interfere constructively. Indeed, for the helicity contributions from both incident and scattered fields, as well as interference, one should have similar signs to sum up constructively.

When both incident and scattered fields are optimally chiral, i.e.,  $\mathbf{E}_{\text{inc}} = \pm i\eta_0 \mathbf{H}_{\text{inc}}$  and  $\mathbf{E}_{\text{sca}} = \pm i\eta_0 \mathbf{H}_{\text{sca}}$ , the total near field is optimally chiral as well, i.e., in phasor terms  $\mathbf{E} = \mathbf{E}_{\text{sca}} + \mathbf{E}_{\text{inc}} = \pm i\eta_0 (\mathbf{H}_{\text{sca}} + \mathbf{H}_{\text{inc}}) = \pm i\eta_0 \mathbf{H}$ . Therefore we illuminate the NA by an optimally chiral beam and devote the rest of this section to investigate the helicity density of the scattered near field  $h_{\text{sca}}$  and to study how the interference between the incident and scattered fields influences the helicity density of the total near field. Later in the paper we discuss the importance of helicity density of the interference between incident and scattered fields.

Without loss of generality, we assume that the NA is isotropic operating in its dipolar regime and model it by the

induced electric and magnetic dipole moments  $\mathbf{p}_{\text{NA}}$  and  $\mathbf{m}_{\text{NA}}$ , respectively, located at the origin of the coordinate system [see Fig. 1(b)]. Therefore scattered electric and magnetic fields at position  $\mathbf{r} = r\hat{\mathbf{r}}$ , where the hat denotes a unit vector, read

$$\mathbf{E}_{\text{sca}} = \left\{ (\hat{\mathbf{r}} \times \mathbf{p}_{\text{NA}}) \times \hat{\mathbf{r}} - c_0^{-1} \left( 1 + \frac{i}{kr} \right) (\hat{\mathbf{r}} \times \mathbf{m}_{\text{NA}}) + \left( \frac{1}{k^2 r^2} - \frac{i}{kr} \right) [3\hat{\mathbf{r}}(\hat{\mathbf{r}} \cdot \mathbf{p}_{\text{NA}}) - \mathbf{p}_{\text{NA}}] \right\} \frac{k^2 e^{ikr}}{4\pi r \epsilon_0} \quad (6)$$

and

$$\mathbf{H}_{\text{sca}} = \left\{ (\hat{\mathbf{r}} \times \mathbf{m}_{\text{NA}}) \times \hat{\mathbf{r}} + c_0 \left( 1 + \frac{i}{kr} \right) (\hat{\mathbf{r}} \times \mathbf{p}_{\text{NA}}) + \left( \frac{1}{r^2 k^2} - \frac{i}{rk} \right) [3\hat{\mathbf{r}}(\hat{\mathbf{r}} \cdot \mathbf{m}_{\text{NA}}) - \mathbf{m}_{\text{NA}}] \right\} \frac{k^2 e^{ikr}}{4\pi r}, \quad (7)$$

respectively, with  $k$  being the wave number in vacuum. These two equations imply that the *scattered* field of the proposed NA is optimally chiral everywhere in space, i.e.,  $\mathbf{E}_{\text{sca}} = \pm i\eta_0 \mathbf{H}_{\text{sca}}$ , hence not only in the near-field zone of the NA, when  $\mathbf{m}_{\text{NA}} = \mp i c_0 \mathbf{p}_{\text{NA}}$ . Therefore the dominant contribution of the helicity density  $h_{\text{sca}}$  of scattered fields in the near zone of the NA at the radial positions  $\mathbf{r} = r\hat{\mathbf{r}}$  reads

$$h_{\text{sca}} \approx \frac{\eta_0}{32\pi^2 \omega r^6} \Im \{ 3(\hat{\mathbf{r}} \cdot \mathbf{p}_{\text{NA}})(\hat{\mathbf{r}} \cdot \mathbf{m}_{\text{NA}}^*) + \mathbf{p}_{\text{NA}} \cdot \mathbf{m}_{\text{NA}}^* \}. \quad (8)$$

Note that in evaluating Eq. (8) for the near field of a NA we have only considered the dominant terms with  $r^{-3}$  dependence. The term  $\Im\{\mathbf{p}_{\text{NA}} \cdot \mathbf{m}_{\text{NA}}^*\}$  in Eq. (8) not only relates helicity to the strength of induced electric and magnetic dipole moments in a NA but also implies that the dipoles relative spatial orientation and phase should be controlled to maximize the helicity density of the scattered near field. Note that when the vector  $r$  is parallel to *both* dipole moments, the term  $\Im\{3(\hat{\mathbf{r}} \cdot \mathbf{p}_{\text{NA}})(\hat{\mathbf{r}} \cdot \mathbf{m}_{\text{NA}}^*)\}$  has a constructive contribution to the enhancement of the helicity density  $h_{\text{sca}}$ . In other words, the location vector  $r$  that satisfies this parallel property defines the regions where helicity around a NA is the strongest.

Electric and magnetic dipole moments induced in a NA are obtained by employing a dielectric NA with high refractive index [27,28,48,66–70]. In what follows we examine thoroughly how to obtain an optimally chiral scattered field when an achiral dielectric NA which does not possess electromagnetic polarizability is irradiated by an optimally chiral beam.

### A. Dielectric NA illuminated by optimally chiral illumination

The dipole moments  $\mathbf{p}_{\text{NA}}$  and  $\mathbf{m}_{\text{NA}}$  are, respectively, related to the incident electric and magnetic fields  $\mathbf{E}_{\text{inc}}^{\circ}$  and  $\mathbf{H}_{\text{inc}}^{\circ}$  at the position of the NA through the electric and magnetic polarizabilities  $\alpha_{\text{ee}}^{\text{NA}}$  and  $\alpha_{\text{mm}}^{\text{NA}}$  of the NA as

$$\mathbf{p}_{\text{NA}} = \alpha_{\text{ee}}^{\text{NA}} \mathbf{E}_{\text{inc}}^{\circ}, \quad \mathbf{m}_{\text{NA}} = \alpha_{\text{mm}}^{\text{NA}} \mathbf{H}_{\text{inc}}^{\circ}. \quad (9)$$

The superscript “ $\circ$ ” denotes the NA’s position, which is the origin of the coordinate system in our example. Since we consider an optimally chiral incident field, i.e.,  $\mathbf{E}_{\text{inc}}^{\circ} = \pm i\eta_0 \mathbf{H}_{\text{inc}}^{\circ}$ , according to Eq. (9), the relation  $\mathbf{m}_{\text{NA}} = \mp i c_0 \mathbf{p}_{\text{NA}}$  holds when the balance relation between the polarizabilities of the NA,

$$\alpha_{\text{ee}}^{\text{NA}} = \epsilon_0 \alpha_{\text{mm}}^{\text{NA}}, \quad (10)$$

known as the first Kerker condition [71], is satisfied. Therefore, based on our previous discussion on Eqs. (6) and (7), the scattered field of the proposed NA (and not only in the near-field zone) is optimally chiral. In other words, the condition in Eq. (10) establishes the occurrence of the best possible scattered near field everywhere, in terms of optimal chirality of light, since the scattered field carries the same helicity of the incident field.

In case the NA has a *chiral* component (i.e., it has an electromagnetic polarizability), the satisfaction of condition (10) still results in an optimally chiral scattered near field when the incident field is optimally chiral, as shown in Appendix. However, a chiral NA unfavorably contributes to the circular dichroism signal in the chirality characterization of a nanoparticle sample [34]. Therefore in this work we focus on describing *achiral* NAs.

Therefore the problem of obtaining the maximum achievable helicity density of the scattered near field at a given energy density is reduced to acquiring a NA that satisfies the balance polarizability relation (10). Such a balance relation implies that the NA simultaneously possesses both electric and magnetic polarizabilities. Though materials with significant magnetic properties are not available at optical frequencies [72], “resonant magnetism” is possible, for example, with plasmonic clusters [45,73–80] or dielectric nanostructures [28,31,67,68,81–90], which supports magneticlike Mie resonances. In the next step, to illustrate in a simple way the proposed concepts, we analyze an isotropic achiral dielectric NA with spherical shape made of high-refractive-index material and investigate the possibility of generating an optimally chiral, total near field around this structure. Moreover, we analyze helicity enhancement due to the scattered and interference fields and demonstrate that they have almost equal importance in enhancing helicity density with respect to that of the excitation beam. Furthermore, we investigate the relation between enhancement in energy and helicity densities in the near field of this NA.

As an example, we assume the spherical NA with radius  $a$  to be made of silicon (Si), and in Fig. 2(a) we plot the logarithm of normalized  $|\alpha_{\text{ee}}^{\text{NA}} - \epsilon_0 \alpha_{\text{mm}}^{\text{NA}}|$  versus wavelength  $\lambda$  and radius  $a$ . The quantity  $|\alpha_{\text{ee}}^{\text{NA}} - \epsilon_0 \alpha_{\text{mm}}^{\text{NA}}|$  is normalized to its maximum in the shown wavelength-radius range, and it vanishes when the balance relation (10) is satisfied, which approximately corresponds to negative large values of its logarithm base 10. Note that polarizabilities take complex values, and the balance relation  $\alpha_{\text{ee}}^{\text{NA}} = \epsilon_0 \alpha_{\text{mm}}^{\text{NA}}$  is satisfied when both magnitudes and phases of  $\alpha_{\text{ee}}^{\text{NA}}$  and  $\epsilon_0 \alpha_{\text{mm}}^{\text{NA}}$  are equal. The difference  $|\alpha_{\text{ee}}^{\text{NA}} - \epsilon_0 \alpha_{\text{mm}}^{\text{NA}}|$  vanishes when the simultaneous satisfaction of equal magnitudes and phases of  $\alpha_{\text{ee}}^{\text{NA}}$  and  $\epsilon_0 \alpha_{\text{mm}}^{\text{NA}}$  is satisfied. Also note that for an efficient NA low losses are desired, and here we assume the dielectric NA to be made of crystalline Si with dielectric permittivity taken from Ref. [81].

Note that when condition (10) approximately holds for a dielectric NA [e.g., on the dark regions in Fig. 2(a)], the scattered near field, and consequently, the total field, is optimally chiral. Moreover, although the spatial distribution of helicity density of the scattered near field is nonuniform around the NA, the relation  $|h| = u/\omega$  holds everywhere in space as long as  $\alpha_{\text{ee}}^{\text{NA}} = \epsilon_0 \alpha_{\text{mm}}^{\text{NA}}$  is valid for the proposed NA. We note that quadrupoles for the considered parameters  $\lambda$  and  $a$  are

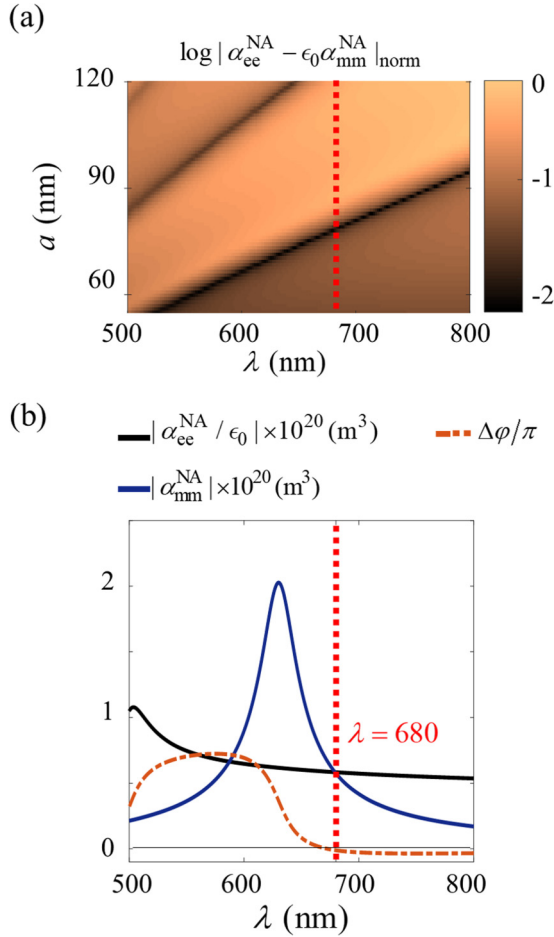


FIG. 2. The polarizabilities of a spherical NA made of Si approximately satisfy the balance relation  $\alpha_{ee}^{\text{NA}} = \epsilon_0 \alpha_{mm}^{\text{NA}}$ . (a) Plot of the logarithm of  $|\alpha_{ee}^{\text{NA}} - \epsilon_0 \alpha_{mm}^{\text{NA}}|$  (normalized to its maximum), which takes negative large value, around -2, where the balance relation  $\alpha_{ee}^{\text{NA}} = \epsilon_0 \alpha_{mm}^{\text{NA}}$  is approximately satisfied, vs radius  $a$  of the NA and wavelength  $\lambda$  of the excitation field. (b) Magnitudes of and phase difference  $\Delta\varphi$  between electric  $\alpha_{ee}^{\text{NA}}$  and magnetic  $\alpha_{mm}^{\text{NA}}$  polarizabilities of a NA with radius  $a = 78$  nm vs wavelength  $\lambda$ . The refractive index of Si is obtained from Ref. [91], and the polarizabilities are calculated using the Mie scattering coefficients [92].

negligible since  $a/\lambda \ll 1$ . In Fig. 2(b) we depict the magnitudes of the electric and magnetic polarizabilities and their normalized phase difference  $\Delta\varphi/\pi$  of a spherical NA made of Si with radius  $a = 78$  nm. At wavelength  $\lambda = 680$  nm both relations  $|\alpha_{ee}^{\text{NA}}| = |\epsilon_0 \alpha_{mm}^{\text{NA}}|$  and  $\Delta\varphi = 0$  are approximately satisfied. This corresponds to a dark region with value of  $-2$  shown in Fig. 2(a). We conclude this section by observing that helicity can be also enhanced without the constraint of having an optically chiral field, as previously observed in the literature using plasmonic NAs [9,13–17,21]. The concept of optimally chiral light is local and implies that at a given point the maximum helicity density is  $|h| = u/\omega$ , where  $u = u_e + u_m$ , with  $u_e = \epsilon_0 |\mathbf{E}|^2/4$  and  $u_m = \mu_0 |\mathbf{H}|^2/4$  denoting the time average electric and magnetic energy densities. When the optimal chirality condition is not met, light locally satisfies  $|h| < u/\omega$  because  $u/\omega$  is the helicity upper bound [34]. In some publications [9,13–17,21] the electric field is

enhanced via plasmonic NAs, leading to an enhancement of both  $u_e$  and possibly also helicity. However, in this case the resulting light is not optically chiral and subject to the bound  $|h| \leq (u_e + u_m)/\omega$ . Furthermore, since this latter case does not constitute optimally chiral light, there are consequences on the determination of chirality through using the dissymmetry factor  $g$  as described in [34]. Finally, we shall also note that helicity at a given electric field energy density  $u_e$  could be enhanced by locally increasing only the magnetic field (i.e., enhancing  $u_m$ ); therefore structured light with an enhanced magnetic field [44,46,66–70,75,93] could be rather important for enhancing helicity.

### III. DIELECTRIC NANOANTENNA UNDER ARPB ILLUMINATION

So far we have shown how to generate optimally chiral near fields—it is required to illuminate a NA by an optimally chiral beam and that the NA has balanced electric and magnetic polarizabilities. Now we discuss some scenarios when a dielectric NA is exposed to an external optimally chiral beam. A trivial example of an optimally chiral field is a Gaussian beam (GB) with circular polarization [30]. Under this illumination, induced dipole moments are transverse to the beam propagation direction, which results in a uniform helicity density distribution in the transverse plane [30]. Here, instead, we analyze helicity density in the near field of a dielectric NA when it is irradiated by an optimally chiral ARPB, and induced dipole moments are oriented along the optical axis of the beam, which leads to a localized helicity density along this axis. The localized helicity density may be used as a nanoprobe to detect chirality at nanoscale using circular dichroism applied to nanoparticles [34] or using photoinduced chiral force microscopy [58,60]. Next, we briefly summarize the pertinent properties of an ARPB.

#### A. Optimally chiral ARPB illumination

The APB and RPB are obtained by superposing Laguerre Gaussian beams with opposite angular momenta [44,46,47,58,60]. The electric field vector (in phasor terms) in an APB propagating along the  $+z$  direction (optical axis of the beam) is polarized along the azimuthal direction  $\hat{\phi}$  in the transverse plane that, after suppressing the time dependence  $\exp(-i\omega t)$ , reads [44]

$$\mathbf{E}^{\text{APB}} = \frac{2V_A \rho}{\sqrt{\pi} w^2} e^{-(\rho/w)^2 \zeta} e^{-2i \tan^{-1}(z/z_R)} e^{ikz} \hat{\phi}, \quad (11)$$

where  $V_A$  (with the unit of volt) is the complex amplitude of the beam. Here,  $z_R = \pi w_0^2/\lambda$ ,  $w = w_0 \sqrt{1 + (z/z_R)^2}$ ,  $\zeta = 1 - iz/z_R$ , and  $R = z [1 + (z_R/z)^2]$ , where  $w_0$  and  $\lambda$  are, respectively, the beam parameter and the excitation wavelength. The beam parameter  $w_0$  represents half of the minimum beam waist when the beam is not tightly focused [44]. Moreover,  $\rho$  is the radial distance from the beam axis (the  $z$  axis). Components of the magnetic field vector in an APB are obtained from a source-free Maxwell's curl equation  $\nabla \times \mathbf{E}^{\text{APB}} =$



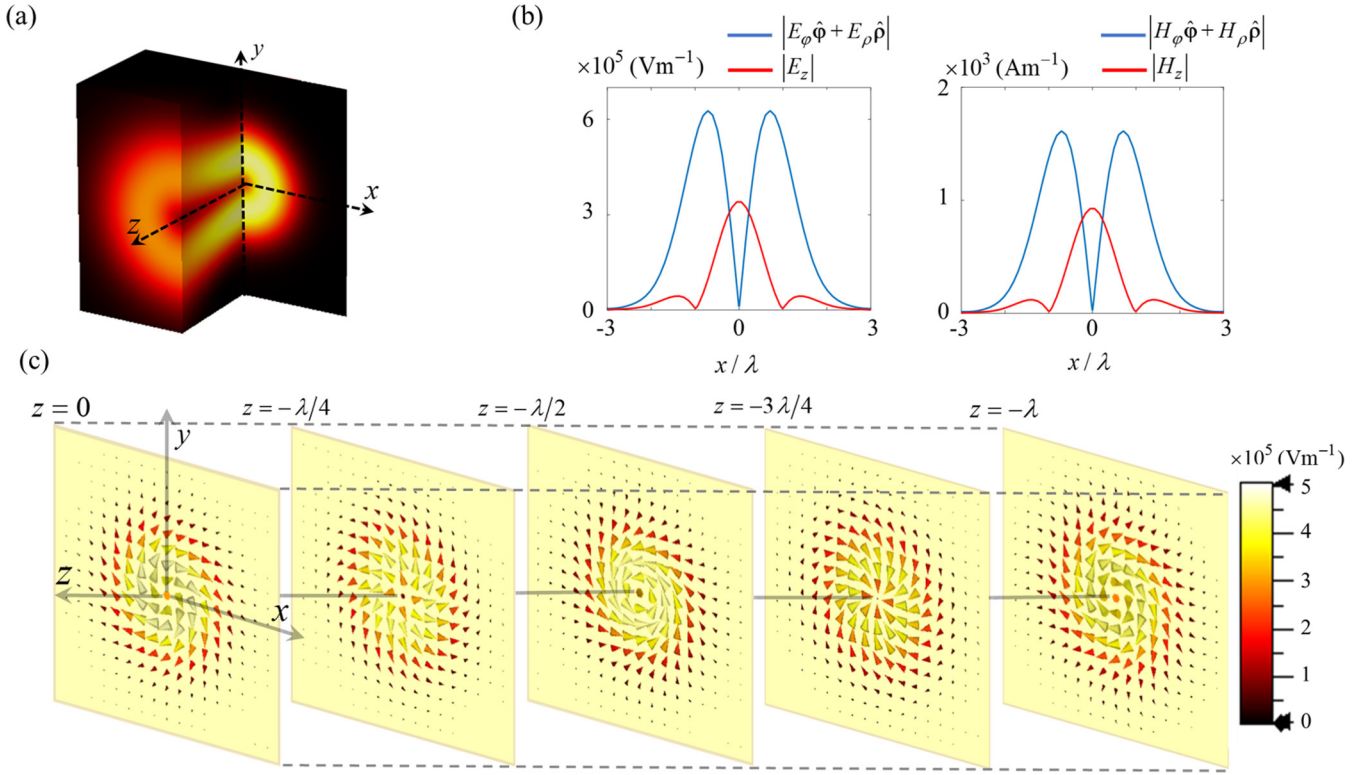


FIG. 3. An optimally chiral ARPB with total power of 1 mW, beam parameter  $w_0 = \lambda$ , and amplitudes  $V_A = \pm iV_R$  propagating along  $z$  direction at wavelength  $\lambda = 680$  nm. (a) Three-dimensional plot of electric field's magnitude  $|E^{\text{ARPB}}|$  in  $x$ - $y$  and  $y$ - $z$  planes. (b) Magnitudes of longitudinal and tangential components of electric and magnetic fields at the minimum waist plane  $z = 0$ . (c) Real part of the electric field vector represented by cones at various  $z = \text{constant}$  planes. The results are obtained via FEM full-wave numerical analysis.

$i\omega\mu_0\mathbf{H}^{\text{APB}}$  and read

$$H_\rho^{\text{APB}} = -\frac{E_\phi^{\text{APB}}}{\eta_0} \left[ 1 + \frac{1}{kz_R} \frac{\rho^2 - 2w_0^2}{w^2} - \frac{4i}{w^2} \frac{z}{z_R} \frac{1}{k^2} \left( 1 - \frac{\rho^2 \zeta}{w^2} \right) \right]$$

$$H_z^{\text{APB}} = \frac{2E_\phi^{\text{APB}}}{i\omega\mu_0\rho} \left( 1 - \frac{\rho^2}{w^2} \zeta \right). \quad (12)$$

It is important to note that such a beam has a vanishing electric field and vanishing *transverse* magnetic fields at its optical axis. Moreover, the longitudinal magnetic field component takes the value  $\lim_{\rho \rightarrow 0} H_z^{\text{APB}} = 4V_A(i\omega\mu_0\sqrt{\pi}w^2)^{-1}e^{-2i\tan^{-1}(z/z_R)}e^{ikz}$  along its optical axis. In summary, around the beam's optical axis, a magnetic dominant region exists.

Dual to the APB, the RPB has magnetic field vectors which are polarized along the azimuthal direction and read

$$\mathbf{H}^{\text{RPB}} = \frac{2V_R\rho}{\eta_0\sqrt{\pi}w^2} e^{-(\rho/w)^2\zeta} e^{-2i\tan^{-1}(z/z_R)} e^{ikz} \hat{\phi}, \quad (13)$$

with a complex amplitude  $V_R$  (with the unit of volt). Components of electric field in an RPB are obtained via source-free Maxwell's curl equation  $\nabla \times \mathbf{H}^{\text{RPB}} = -i\omega\epsilon_0\mathbf{E}^{\text{RPB}}$  and read

$$E_\rho^{\text{RPB}} = \eta_0 H_\phi^{\text{RPB}} \left[ 1 + \frac{1}{kz_R} \frac{\rho^2 - 2w_0^2}{w^2} - \frac{4i}{w^2} \frac{z}{z_R} \frac{1}{k^2} \left( 1 - \frac{\rho^2 \zeta}{w^2} \right) \right]$$

$$E_z^{\text{RPB}} = -\frac{2H_\phi^{\text{RPB}}}{i\omega\epsilon_0\rho} \left( 1 - \frac{\rho^2}{w^2} \zeta \right). \quad (14)$$

Note, an RPB has a nonzero longitudinal electric field component  $\lim_{\rho \rightarrow 0} E_z^{\text{RPB}} = ic_0 4V_R(\omega\sqrt{\pi}w^2)^{-1}e^{-2i\tan^{-1}(z/z_R)}e^{ikz}$  along its axis [44,58,94], where the magnetic field  $\mathbf{H}^{\text{RPB}}$  and the transverse component of the electric field  $E_\rho^{\text{RPB}}$  vanish.

The ARPB is the superposition of these two vortex beams, i.e.,

$$\mathbf{E}^{\text{ARPB}} = \mathbf{E}^{\text{APB}} + \mathbf{E}^{\text{RPB}}, \quad \mathbf{H}^{\text{ARPB}} = \mathbf{H}^{\text{APB}} + \mathbf{H}^{\text{RPB}}, \quad (15)$$

with the same beam parameters. Indeed, it is easy to deduce that an ARPB possesses both electric and magnetic field components along the azimuth direction  $\hat{\phi}$ , as well as along the radial and longitudinal directions  $\hat{\rho}$  and  $\hat{z}$ . Moreover, since  $\mathbf{E}^{\text{APB}} = \eta_0 V_A V_R^{-1} \mathbf{H}^{\text{RPB}}$ , Eq. (15) simplifies to

$$\mathbf{E}^{\text{ARPB}} = \eta_0 V_A V_R^{-1} \mathbf{H}^{\text{RPB}} + \mathbf{E}^{\text{RPB}}$$

$$\mathbf{H}^{\text{ARPB}} = \mathbf{H}^{\text{RPB}} + \eta_0^{-1} V_A^{-1} V_R \mathbf{E}^{\text{RPB}}, \quad (16)$$

which shows that electric and magnetic field components of an ARPB are linked through  $\mathbf{E}^{\text{ARPB}} = \eta_0 V_A V_R^{-1} \mathbf{H}^{\text{ARPB}}$ . Therefore, when the amplitudes satisfy  $V_A = \pm iV_R$ , the ARPB constitutes an optimally chiral optical beam that satisfies condition (1) everywhere in space (under paraxial approximation) because  $V_A V_R^{-1} = \pm i$ .

In Fig. 3(a) the electric field magnitude  $|E^{\text{ARPB}}|$  of an optimally chiral ARPB with  $V_A = \pm iV_R$  propagating along the  $z$  direction with total power of 1 mW and beam parameter  $w_0 = \lambda$  is depicted. The plot is obtained by a full-wave simulation using the finite element method (FEM) implemented in the CST STUDIO SUITE at wavelength  $\lambda = 680$  nm. One interesting

feature of an ARPB is that it has exclusively longitudinal electric  $E_z^{\text{ARPB}}$  and magnetic  $H_z^{\text{ARPB}}$  fields on the beam axis. In Fig. 3(b) the magnitude of longitudinal and transverse components of electric and magnetic fields in the same ARPB in Fig. 3(a) are depicted at the minimum waist plane of the beam (here the  $z = 0$  plane). Moreover, the real part of the electric-field-vector component of the same beam at various  $z = \text{constant}$  planes is illustrated in Fig. 3(c).

In summary, the electric and magnetic fields have a phase shift of  $\pm\pi/2$ , everywhere, in their longitudinal and transverse components. In particular, we stress that the purely longitudinal field components on the beam axis are phase shifted by  $\pm\pi/2$  and form an optimally chiral field. Indeed, helicity density on the axis of ARPB illumination, and at its minimum waist, reads

$$h_{\text{inc}} = \frac{\mu_0}{2\omega} |\mathbf{H}^{\text{ARPB}}|^2 \Im\{V_A V_R^{-1}\} = \frac{2u_m}{\omega} \Im\{V_A V_R^{-1}\}, \quad (17)$$

or equivalently,

$$h_{\text{inc}} = -\frac{\epsilon_0}{2\omega} |\mathbf{E}^{\text{ARPB}}|^2 \Im\{V_R V_A^{-1}\} = \frac{-2u_e}{\omega} \Im\{V_A^{-1} V_R\}, \quad (18)$$

which shows that

$$h_{\text{inc}} = \pm \frac{2u_{e,\text{inc}}}{\omega} = \pm \frac{2u_{m,\text{inc}}}{\omega} = \pm \frac{u_{\text{inc}}}{\omega} \quad (19)$$

when  $V_A = \pm iV_R$ . Here  $u_{e,\text{inc}}$ ,  $u_{m,\text{inc}}$ , and  $u_{\text{inc}}$  are, respectively, electric, magnetic, and total energy densities of the incident ARPB.

### B. Helicity maximization in near field of a spherical dielectric NA under ARPB illumination

We consider a situation where a spherical Si NA with polarizabilities which satisfy condition (10) is illuminated by an optimally chiral ARPB propagating in the  $+z$  direction with half-beam waist parameter  $w_0 = \lambda$ . The optical axis of the beam coincides with the  $z$  axis, and on this axis its electric and magnetic fields vectors are purely longitudinal, i.e., parallel to each other (in phasor terms), and form an optimally chiral incident field. Hence the induced electric and magnetic dipole moments  $\mathbf{p}_{\text{NA}}$  and  $\mathbf{m}_{\text{NA}}$  in the dielectric NA are *parallel* to the  $z$  axis under such an illumination, and the helicity density of the scattered near field, introduced in Eq. (8), at location  $(r, \theta, \phi)$  near the NA reads

$$h_{\text{sca}} \approx \frac{|\mathbf{E}_{\text{inc}}^{\text{o}}|^2}{32\pi^2 \omega r^6} (3\cos^2\theta + 1) \Re\{\alpha_{\text{ee}}^{\text{NA}} (\alpha_{\text{mm}}^{\text{NA}})^*\}. \quad (20)$$

Now we define the *helicity enhancement factor*  $|h_{\text{sca}}|/|h_{\text{inc}}^{\text{o}}|$ , which is the ratio of *scattered* near-field helicity density  $h_{\text{sca}}$  to the helicity density of the incident field at the origin, where the NA is located. Note that normalizing scattered helicity density to that of the incident field at the position of the NA,  $h_{\text{inc}}^{\text{o}}$ , eliminates the influence of the incident field intensity from the enhancement factor  $|h_{\text{sca}}|/|h_{\text{inc}}^{\text{o}}|$ . Since the electric

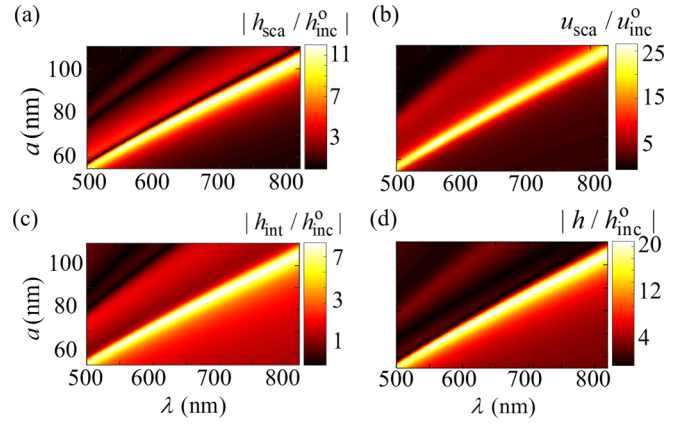


FIG. 4. Enhancement of (a) helicity and (b) energy densities of the *scattered* field on the surface of a Si NA, evaluated along the  $+z$  direction, i.e., at  $\mathbf{r} = a\hat{\mathbf{z}}$ , when illuminated by an optimally chiral ARPB propagating along the positive  $z$  direction with beam's half-waist parameter  $w_0 = \lambda$ . They are normalized with respect to the analogous densities of the incident ARPB evaluated at the origin. The very bright region represents the area where scattered helicity density is 11 times larger than that of the incident ARPB beam at its axis. Helicity and energy enhancements occur in regions close to each other. Interference (c) and total (d) helicity densities, both normalized to that of the incident ARPB beam, evaluated at  $\mathbf{r} = a\hat{\mathbf{z}}$ . The maximum of total helicity density enhancement  $|h/h_{\text{inc}}^{\text{o}}|$  is approximately 20. The plots also show that the interference helicity density  $h_{\text{int}}$  in Eq. (22) has a considerable contribution to the total helicity enhancement. That is why it is important that the interference term has the same sign of the scattered and incident helicities.

$\mathbf{E}_{\text{inc}}$  and magnetic  $\mathbf{H}_{\text{inc}}$  components of the incident field satisfy  $\mathbf{E}_{\text{inc}} = \pm i\eta_0 \mathbf{H}_{\text{inc}}$ , the magnitude of helicity density of the incident field at the position of the NA reads  $|h_{\text{inc}}^{\text{o}}| = |\mathbf{E}_{\text{inc}}^{\text{o}}| |\mathbf{H}_{\text{inc}}^{\text{o}}| / (2\omega c_0)$ . Consequently, the helicity enhancement

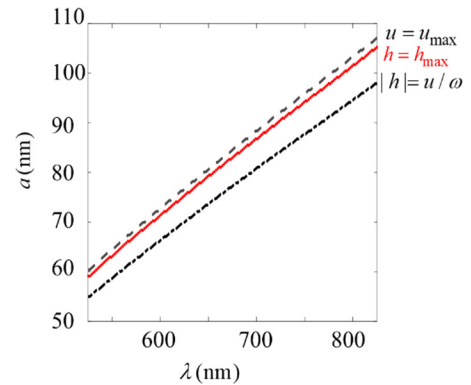


FIG. 5. Radius of the dielectric NA that guarantees the maximum enhancement of energy density  $u_{\text{max}}$ , maximum helicity density  $h_{\text{max}}$ , and the “optimal chirality” condition  $|h| = u/\omega$  to be satisfied vs free-space wavelength  $\lambda$ . In all cases the power of the incident field is kept constant. Note that for a chosen operating wavelength, the maximum of helicity enhancement, energy enhancement, and the condition  $\alpha_{\text{ee}}^{\text{NA}} = \epsilon_0 \alpha_{\text{mm}}^{\text{NA}}$  (for optimal near-field chirality) occur at different radii of the dielectric NA. Maximum helicity enhancement occurs at radial values between the other two.

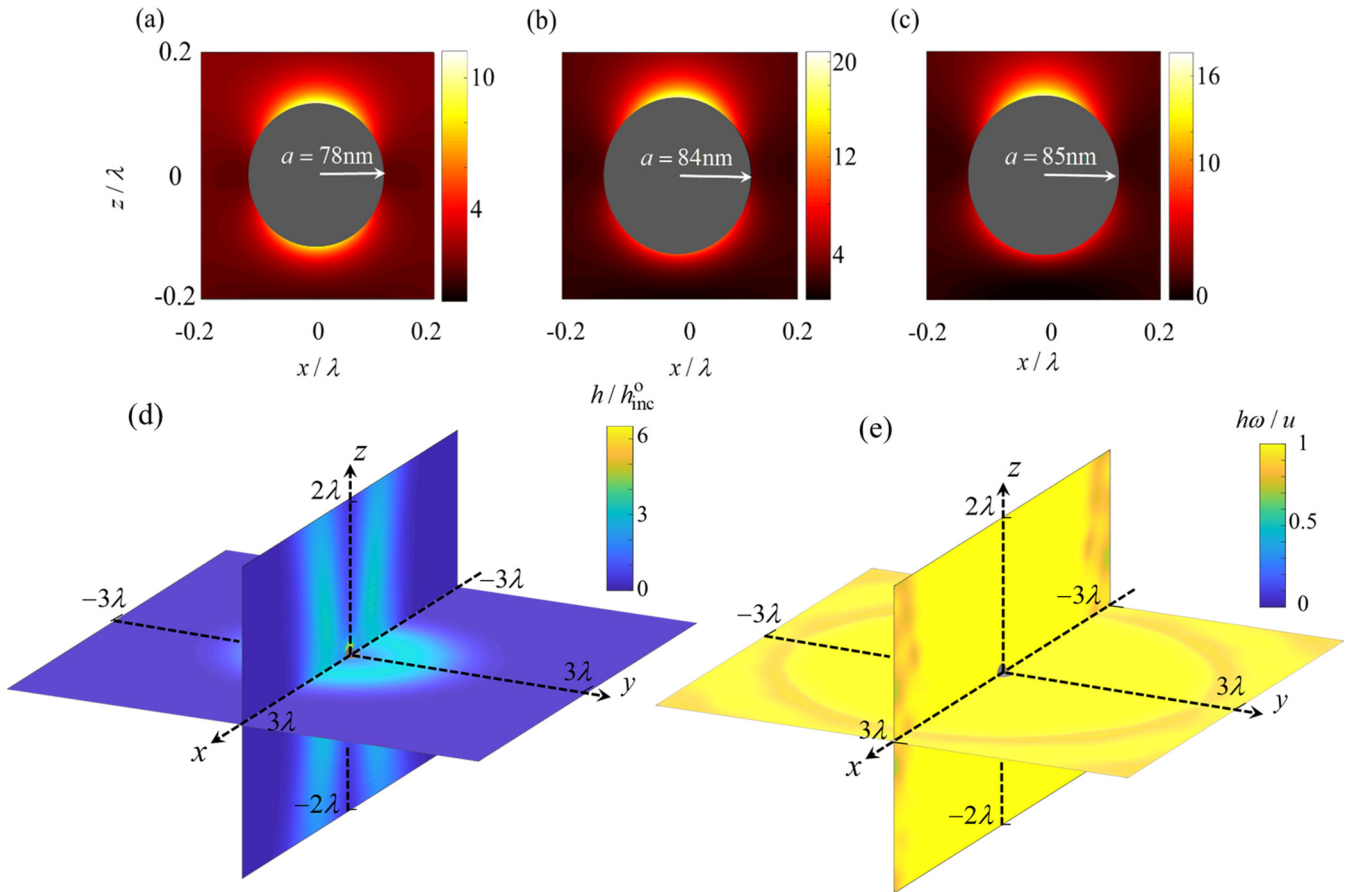


FIG. 6. Total helicity enhancement  $h/h_{\text{inc}}^o$  around a spherical Si NA in the  $x$ - $z$  plane under optimally chiral ARPB illumination with half-waist  $w_0 = \lambda$ , obtained by free-space Green's functions and Mie scattering calculations at  $\lambda = 680$  nm. At this wavelength, for a dielectric NA with radius  $a = 78$  nm (a), the optimal chirality condition (1) is satisfied in the near field, whereas for  $a = 84$  nm (b) and  $a = 85$  nm (c) the maximum helicity and maximum energy enhancements are obtained, respectively. Maximum helicity enhancement occurs for a radius between that corresponding to the optimally chiral near field and that corresponding to maximum energy density. In (d) and (e) helicity enhancement and the quantity  $h\omega/u$ , which takes the value of  $+1$  for an optimally chiral ARPB, with  $V_A = iV_R$  around the Si NA with radius 78 nm obtained from FEM analysis are plotted.

due to scattered near field of the NA is approximated as

$$\frac{|h_{\text{sca}}|}{|h_{\text{inc}}^o|} \approx \frac{1}{16\epsilon_0\pi^2r^6}(3\cos^2\theta + 1)|\Re\{\alpha_{\text{ec}}^{\text{NA}}(\alpha_{\text{mm}}^{\text{NA}})^*\}|. \quad (21)$$

It is clear from Eq. (21) that the maximum helicity density occurs at  $\theta = 0, \pi$ , i.e., along the  $z$  direction, since both moments  $\mathbf{p}_{\text{NA}}$  and  $\mathbf{m}_{\text{NA}}$  are oriented along  $z$ .

To investigate the influence of satisfaction of condition (10) and the relation between energy and helicity density enhancements in an optimally chiral near field around a spherical Si NA, we also define the *energy enhancement ratio*  $u_{\text{sca}}/u_{\text{inc}}^o$  as the time-averaged energy density of the scattered near field at a desired location with respect to that of the incident field at the origin, i.e., at the center of the NA. Figures 4(a) and 4(b) depict energy and helicity density enhancements. These plots show that helicity and energy density enhancements in the scattered field around the Si NA follow the same trends. Note that in Eq. (21) we only considered the dominant terms of the near field of the NA, generated by the superposition of an electric and a magnetic dipole, to provide a simple analytical formula. However, the values demonstrated in Figs. 4(a) and

4(b) include all the terms of the dynamic Green's function for completeness, and we note that these values are very close to those provided by the approximate formula given in Eq. (21).

To investigate further, using the evaluated time-averaged helicity and energy densities at the surface of the NA at  $\mathbf{r} = a\hat{\mathbf{z}}$ , in Fig. 5 we plot the required radius of the NA versus excitation wavelength  $\lambda$  to enforce (a) that the balance relation (10) leading to an optimally chiral field is satisfied, which is equivalent to having a scattered near field satisfying the condition  $|h_{\text{sca}}| = u_{\text{sca}}/\omega$ ; (b) the maximum helicity enhancement  $h_{\text{max}}$ ; and (c) the maximum energy density enhancement  $u_{\text{max}}$ . In all the cases the power of the incident ARPB is kept constant.

As it is clear from this figure, at each wavelength the maximum helicity and energy densities  $h_{\text{max}}$  and  $u_{\text{max}}$  do not occur at the same NA radius. Indeed, the concept of optimal chirality refers to  $|h| = u/\omega$ , since we know that at given frequency,  $|h|$  cannot be larger than  $|h| = u/\omega$ . On the other hand, for other radius values, the energy density is locally increased, whereas at a given radius  $|h|$  it is maximum (though with  $|h| < u/\omega$ ). This is why the two curves of maximum  $|h|$  and maximum  $|u|$  are close to each other. In the case of a spherical



dielectric NA, at the radius where the maximum of energy density enhancement occurs, condition (1) is not precisely satisfied, which means that although the energy density of the field is enhanced considerably, helicity density does not reach its upper bound  $|h| = u/\omega$ . (Again, the upper bound denotes the “optimal chirality” of light [34].) Note that the maximum helicity density  $h_{\max}$  curve is located between the curve of  $u_{\max}$  and that corresponding to the optimal chirality condition  $|h| = u/\omega$ . Moreover, the curve corresponding to the optimally chiral field, i.e.,  $|h| = u/\omega$ , does not cross the curve associated to  $h_{\max}$ .

So far we have discussed helicity enhancement due to the scattering near field of the NA. However, the overall helicity density of the field around the NA is determined by Eq. (4). In the following we discuss the importance of the *interference* term  $h_{\text{int}}$  [see Eq. (5)] to total helicity enhancement.

Under the balance relation (10) for NAs and considering the optimally chiral ARPB excitation, interference helicity density in Eq. (5) reduces to

$$h_{\text{int}} = \frac{1}{4\pi\omega r^3} \Re \left\{ e^{ikr} \alpha_{\text{ee}}^{\text{NA}} \left[ 3(\hat{\mathbf{r}} \cdot \mathbf{E}_{\text{inc}}^*) (\hat{\mathbf{r}} \cdot \mathbf{E}_{\text{inc}}^{\circ}) - \mathbf{E}_{\text{inc}}^{\circ} \cdot \mathbf{E}_{\text{inc}}^* \right] \right\}. \quad (22)$$

We recall that here  $\mathbf{E}_{\text{inc}}$  is the incident field at the location where helicity is evaluated, while  $\mathbf{E}_{\text{inc}}^{\circ}$  is the incident field at the center of the NA.

Total helicity enhancement is given by

$$\left| \frac{h}{h_{\text{inc}}} \right| = \left| 1 + \frac{h_{\text{sca}}}{h_{\text{inc}}} + \frac{h_{\text{int}}}{h_{\text{inc}}} \right|. \quad (23)$$

Enhancement of both interference helicity density  $|h_{\text{int}}/h_{\text{inc}}^{\circ}|$  and total helicity density  $|h/h_{\text{inc}}^{\circ}|$ , evaluated at the surface of the NA along the  $+z$  direction, i.e., at  $\mathbf{r} = a\hat{\mathbf{z}}$ , is illustrated in Figs. 4(c) and 4(d). As it is obvious from this figure, although the enhancement contribution due to interference helicity  $h_{\text{int}}$  is weaker than that associated to the scattering field in Figs. 4(a) and 4(b), its contribution is not negligible in the total helicity enhancement and must be considered in computations and in NA engineering. It is also important to say that to maximize helicity density it is convenient to have the sign of the *interference* helicity density term equal to that of the scattered and incident helicities.

Finally, three illustrative NAs with three NA radii of  $a = 78, 84,$  and  $85$  nm are considered in Fig. 6, at the operational wavelength of  $\lambda = 680$  nm. These three values are chosen from Fig. 5 because at this wavelength they respectively generate (a) the optimum chirality condition  $|h| = u/\omega$ , (b) the maximum enhanced total helicity  $|h/h_{\text{inc}}^{\circ}|$ , and (c) the maximum enhanced energy  $u_{\max}/u_{\text{inc}}^{\circ}$ . The figure shows the distribution of the helicity densities around the dielectric NA. As it is clear, a 20-fold enhancement of helicity density, localized at  $\mathbf{r} = a\hat{\mathbf{z}}$ , is achieved with a spherical dielectric NA with a radius of  $a = 84$  nm. Note that this value is larger than the 10-fold enhancement obtained with the optimum chirality condition ( $|h| = u/\omega$ ), because at radius  $a = 84$  nm one has larger energy density  $u$ , though satisfying the condition  $|h| < u/\omega$ . Maximum helicity enhancement occurs for a radius between that corresponding to the optimally chiral near field and that corresponding to maximum energy density.

The radii generating maximum helicity and maximum energy density are very close to each other.

In parts (d) and (e) of Fig. 6 we plot the helicity enhancement and the quantity  $h\omega/u$ , which takes  $+1$  for an optimally chiral ARPB with  $V_A = iV_R$  around a spherical Si NA with radius  $a = 78$  nm obtained by FEM analysis with the CST STUDIO SUITE at wavelength  $\lambda = 680$  nm.

#### IV. CONCLUSION

We have presented an analysis of helicity density in the near field of a dielectric achiral NA and proved that a NA with *balanced* electric and magnetic dipole moments, i.e.,  $\mathbf{m}_{\text{NA}} = \pm ic_0 \mathbf{p}_{\text{NA}}$ , generates an *optimally chiral* scattered near field everywhere. To have an optimally chiral near field we have used an optimally chiral excitation, and under this condition, balanced electric and magnetic polarizabilities  $\alpha_{\text{ee}}^{\text{NA}} = \epsilon_0 \alpha_{\text{mm}}^{\text{NA}}$  guarantee that  $\mathbf{m}_{\text{NA}} = \pm ic_0 \mathbf{p}_{\text{NA}}$ . The dipolar polarizabilities of a spherical high-density dielectric NA mainly satisfy this requirement when the NA’s radius is chosen appropriately. Furthermore, upon illumination of a dielectric NA by an optimally chiral ARPB, which is a combination of azimuthally and radially polarized vortex beams with electric and magnetic fields with a 90-deg phase difference and appropriate relative amplitudes, we have demonstrated that the NA’s near field is optimally chiral, i.e., it satisfies Eq. (1) everywhere in space. The optimally chiral longitudinal fields of the ARPB generate parallel magnetic and electric dipoles that generate optimally chiral scattered fields. We have shown that the NA’s near field localizes helicity density below the diffraction limit and that helicity is enhanced by more than an order of magnitude compared to that of the illuminating chiral field. These findings enable possible realizations of efficient NAs for chirality characterization at nanoscale.

We have observed that helicity can be enhanced even more than what is possible with the constraint of having an optimally chiral field but at the expense of having a higher energy density. For example, plasmonic NAs may locally enhance helicity but they strongly enhance electric field energy density as well; the enhancement of electric energy density is larger than the enhancement in helicity when structured light is not optically chiral. Optimally chiral fields are important when one desires to obtain the maximum possible helicity while keeping a low electric field that could alter the specimen to be detected or even the detection scheme. Another advantage of using illuminations and NAs that provide optimal chiral light is the simplification of the expression of the dissymmetry factor  $g$ , as explained in Ref. [34].

#### ACKNOWLEDGMENT

The authors acknowledge support by the W. M. Keck Foundation, USA. The authors are thankful to DS SIMULIA for providing CST Studio Suite that was instrumental in this study.

#### APPENDIX: OPTIMALLY CHIRAL SCATTERED NEAR FIELD OF A CHIRAL NA

In the literature there are a few notations to define magnetic dipoles and polarizabilities. In this paper we use the SI unit system, and the magnetic dipole moment induced in the NA is



defined as  $\mathbf{m} = \frac{1}{2} \int_V \mathbf{r} \times \mathbf{J}(\mathbf{r}) dv$ , where  $J(r)$  is displacement current density in the NA, and as a consequence, the magnetic polarizability has unit of  $m^3$ .

In a reciprocal *chiral* NA, the dipole moments  $\mathbf{p}_{\text{NA}}$  and  $\mathbf{m}_{\text{NA}}$  are related to the incident electric and magnetic fields  $\mathbf{E}_{\text{inc}}^o$  and  $\mathbf{H}_{\text{inc}}^o$  at the position of the NA as

$$\begin{aligned} \mathbf{p}_{\text{NA}} &= \alpha_{\text{ee}}^{\text{NA}} \mathbf{E}_{\text{inc}}^o + \alpha_{\text{em}}^{\text{NA}} \mathbf{H}_{\text{inc}}^o, \\ \mathbf{m}_{\text{NA}} &= \alpha_{\text{mm}}^{\text{NA}} \mathbf{H}_{\text{inc}}^o - \mu_0^{-1} \alpha_{\text{em}}^{\text{NA}} \mathbf{E}_{\text{inc}}^o, \end{aligned} \quad (\text{A1})$$

where  $\alpha_{\text{em}}^{\text{NA}}$  is the electromagnetic polarizability of the NA and represents its chirality. The relation  $\mathbf{m}_{\text{NA}} = \mp i c_0 \mathbf{p}_{\text{NA}}$  holds when

$$\alpha_{\text{mm}}^{\text{NA}} \mathbf{H}_{\text{inc}}^o - \mu_0^{-1} \alpha_{\text{em}}^{\text{NA}} \mathbf{E}_{\text{inc}}^o = \mp i c_0 (\alpha_{\text{ee}}^{\text{NA}} \mathbf{E}_{\text{inc}}^o + \alpha_{\text{em}}^{\text{NA}} \mathbf{H}_{\text{inc}}^o). \quad (\text{A2})$$

When the NA is illuminated by an optimally chiral incident field, i.e., when  $\mathbf{E}_{\text{inc}}^o = \pm i \eta_0 \mathbf{H}_{\text{inc}}^o$ , after some algebraic calculations, Eq. (A2) simplifies to

$$(\alpha_{\text{mm}}^{\text{NA}} \mp i c_0 \alpha_{\text{em}}^{\text{NA}}) \mathbf{H}_{\text{inc}}^o = (\epsilon_0 \alpha_{\text{ee}}^{\text{NA}} \mp i c_0 \alpha_{\text{em}}^{\text{NA}}) \mathbf{H}_{\text{inc}}^o. \quad (\text{A3})$$

This is then reduced to  $\alpha_{\text{mm}}^{\text{NA}} \mathbf{H}_{\text{inc}}^o = \epsilon_0 \alpha_{\text{ee}}^{\text{NA}} \mathbf{H}_{\text{inc}}^o$ , which is satisfied when  $\alpha_{\text{ee}}^{\text{NA}} = \epsilon_0 \alpha_{\text{mm}}^{\text{NA}}$ . In summary, dipole moments of a *chiral* NA satisfy  $\mathbf{m}_{\text{NA}} = \mp i c_0 \mathbf{p}_{\text{NA}}$  when (i)  $\alpha_{\text{ee}}^{\text{NA}} = \epsilon_0 \alpha_{\text{mm}}^{\text{NA}}$  and (ii) an optimally chiral field is used to illuminate the NA. Therefore the near field of a chiral NA is optimally chiral under these two conditions. Note that these are the same conditions that an achiral NA should satisfy to generate an optically chiral scattered near field and far field.

- 
- [1] J. P. Riehl, *Mirror-Image Asymmetry: An Introduction to the Origin and Consequences of Chirality* (John Wiley & Sons, New York, 2011).
- [2] G. H. Wagnière, *On Chirality and the Universal Asymmetry: Reflections on Image and Mirror Image* (John Wiley & Sons, Zurich, Switzerland, 2008).
- [3] R. J. Crossley, *Chirality and Biological Activity of Drugs* (CRC Press, Boca Raton, FL, 1995).
- [4] D. B. Amabilino, *Chirality at the Nanoscale: Nanoparticles, Surfaces, Materials and More* (John Wiley & Sons, VCH Verlag GmbH & Co. KGaA, 2009).
- [5] L. D. Barron, *Chirality* **24**, 879 (2012).
- [6] Y. Tang and A. E. Cohen, *Science* **332**, 333 (2011).
- [7] A. O. Govorov, Z. Fan, P. Hernandez, J. M. Slocik, and R. R. Naik, *Nano Lett.* **10**, 1374 (2010).
- [8] B. Auguie, J. L. Alonso-Gómez, A. Guerrero-Martínez, and L. M. Liz-Marzán, *J. Phys. Chem. Lett.* **2**, 846 (2011).
- [9] M. Schäferling, D. Dregely, M. Hentschel, and H. Giessen, *Phys. Rev. X* **2**, 031010 (2012).
- [10] A. O. Govorov and Z. Fan, *Chem. Phys. Chem.* **13**, 2551 (2012).
- [11] N. A. Abdulrahman, Z. Fan, T. Tonooka, S. M. Kelly, N. Gadegaard, E. Hendry, A. O. Govorov, and M. Kadodwala, *Nano Lett.* **12**, 977 (2012).
- [12] X. Yin, M. Schäferling, B. Metzger, and H. Giessen, *Nano Lett.* **13**, 6238 (2013).
- [13] N. Meinzer, E. Hendry, and W. L. Barnes, *Phys. Rev. B* **88**, 041407(R) (2013).
- [14] B. Frank, X. Yin, M. Schäferling, J. Zhao, S. M. Hein, P. V. Braun, and H. Giessen, *ACS Nano* **7**, 6321 (2013).
- [15] V. K. Valev, J. J. Baumberg, C. Sibilia, and T. Verbiest, *Adv. Mater.* **25**, 2517 (2013).
- [16] D. Lin and J.-S. Huang, *Opt. Express* **22**, 7434 (2014).
- [17] M. Schäferling, X. Yin, N. Engheta, and H. Giessen, *ACS Photonics* **1**, 530 (2014).
- [18] X. Yin, M. Schäferling, A.-K. U. Michel, A. Tittl, M. Wuttig, T. Taubner, and H. Giessen, *Nano Lett.* **15**, 4255 (2015).
- [19] G. Armelles, A. Cebollada, H. Y. Feng, A. García-Martín, D. Meneses-Rodríguez, J. Zhao, and H. Giessen, *ACS Photonics* **2**, 1272 (2015).
- [20] X. Duan, S. Kamin, F. Sterl, H. Giessen, and N. Liu, *Nano Lett.* **16**, 1462 (2016).
- [21] M. Schäferling, N. Engheta, H. Giessen, and T. Weiss, *ACS Photonics* **3**, 1076 (2016).
- [22] C. Kramer, M. Schäferling, T. Weiss, H. Giessen, and T. Brixner, *ACS Photonics* **4**, 396 (2017).
- [23] M. Hentschel, M. Schäferling, X. Duan, H. Giessen, and N. Liu, *Sci. Adv.* **3**, e1602735 (2017).
- [24] G. Pellegrini, M. Finazzi, M. Celebrano, L. Duò, and P. Biagioni, *Chirality* **30**, 883 (2018).
- [25] E. S. A. Goerlitzer, R. Mohammadi, S. Nechayev, P. Banzer, and N. Vogel, *Adv. Opt. Mater.* **7**, 1801770 (2019).
- [26] F. Graf, J. Feis, X. Garcia-Santiago, M. Wegener, C. Rockstuhl, and I. Fernandez-Corbaton, *ACS Photonics* **6**, 482 (2019).
- [27] M. Hanifeh and F. Capolino, *J. Appl. Phys.* **127**, 093104 (2020).
- [28] C.-S. Ho, A. Garcia-Etxarri, Y. Zhao, and J. Dionne, *ACS Photonics* **4**, 197 (2017).
- [29] M. L. Solomon, J. Hu, M. Lawrence, A. García-Etxarri, and J. A. Dionne, *ACS Photonics* **6**, 43 (2019).
- [30] M. Hanifeh, M. Albooyeh, and F. Capolino, *Proc. SPIE* **10935**, 1093504 (2019).
- [31] A. García-Etxarri and J. A. Dionne, *Phys. Rev. B* **87**, 235409 (2013).
- [32] A. Vázquez-Guardado and D. Chanda, *Phys. Rev. Lett.* **120**, 137601 (2018).
- [33] K. Y. Bliokh, A. Y. Bekshaev, and F. Nori, *New J. Phys.* **15**, 033026 (2013).
- [34] M. Hanifeh, M. Albooyeh, and F. Capolino, *ACS Photonics* **7**, 2682 (2020).
- [35] R. P. Cameron, S. M. Barnett, and A. M. Yao, *New J. Phys.* **14**, 053050 (2012).
- [36] M. Nieto-Vesperinas, *Philos. Trans. R. Soc. A* **375**, 20160314 (2017).
- [37] A. F. Ranada, *Eur. J. Phys.* **13**, 70 (1992).
- [38] J. L. Trueba and A. F. Rañada, *Eur. J. Phys.* **17**, 141 (1996).
- [39] M. Nieto-Vesperinas, *J. Opt.* **19**, 065402 (2017).
- [40] P. Gutsche and M. Nieto-Vesperinas, *Sci. Rep.* **8**, 9416 (2018).
- [41] M. Nieto-Vesperinas, *Phys. Rev. A* **100**, 023812 (2019).
- [42] W. Kuhn, *Annu. Rev. Phys. Chem.* **9**, 417 (1958).
- [43] Y. Tang and A. E. Cohen, *Phys. Rev. Lett.* **104**, 163901 (2010).
- [44] M. Veysi, C. Guclu, and F. Capolino, *J. Opt. Soc. Am. B: Opt. Phys.* **33**, 2265 (2016).
- [45] C. Guclu, M. Veysi, and F. Capolino, *ACS Photonics* **3**, 2049 (2016).

- [46] J. Zeng, F. Huang, C. Guclu, M. Veysi, M. Albooyeh, H. K. Wickramasinghe, and F. Capolino, *ACS Photonics* **5**, 390 (2018).
- [47] M. Rajaei, M. A. Almajhadi, J. Zeng, and H. K. Wickramasinghe, *Opt. Express* **26**, 26365 (2018).
- [48] J. Zeng, M. Darvishzadeh-Varcheie, M. Albooyeh, M. Rajaei, M. Kamandi, M. Veysi, E. O. Potma, F. Capolino, and H. K. Wickramasinghe, *ACS Nano* **12**, 12159 (2018).
- [49] A. Holleczeck, A. Aiello, C. Gabriel, C. Marquardt, and G. Leuchs, *Opt. Express* **19**, 9714 (2011).
- [50] R. Oron, S. Blit, N. Davidson, A. A. Friesem, Z. Bomzon, and E. Hasman, *Appl. Phys. Lett.* **77**, 3322 (2000).
- [51] H. Rubinsztein-Dunlop, A. Forbes, M. V. Berry, M. R. Dennis, D. L. Andrews, M. Mansuripur, C. Denz, C. Alpmann, P. Banzer, T. Bauer, E. Karimi, L. Marrucci, M. Padgett, M. Ritsch-Marte, N. M. Litchinitser, N. P. Bigelow, C. Rosales-Guzmán, A. Belmonte, J. P. Torres, T. W. Neely *et al.*, *J. Opt.* **19**, 013001 (2017).
- [52] A. V. Nesterov and V. G. Niziev, *J. Phys. D: Appl. Phys.* **33**, 1817 (2000).
- [53] D. Deng, *J. Opt. Soc. Am. B: Opt. Phys.* **23**, 1228 (2006).
- [54] R. Dorn, S. Quabis, and G. Leuchs, *Phys. Rev. Lett.* **91**, 233901 (2003).
- [55] Y. Kozawa and S. Sato, *Opt. Lett.* **30**, 3063 (2005).
- [56] E. Y. S. Yew and C. J. R. Sheppard, *Opt. Lett.* **32**, 3417 (2007).
- [57] A. V. Nesterov, V. G. Niziev, and V. P. Yakunin, *J. Phys. D: Appl. Phys.* **32**, 2871 (1999).
- [58] M. Kamandi, M. Albooyeh, M. Veysi, M. Rajaei, J. Zeng, H. K. Wickramasinghe, and F. Capolino, *ACS Photonics* **5**, 4360 (2018).
- [59] J. S. Eismann, M. Neugebauer, and P. Banzer, *Optica* **5**, 954 (2018).
- [60] J. Zeng, M. Kamandi, M. Darvishzadeh-Varcheie, M. Albooyeh, M. Veysi, C. Guclu, M. Hanifeh, M. Rajaei, E. O. Potma, H. K. Wickramasinghe, and F. Capolino, *EPJ Appl. Metamater.* **5**, 7 (2018).
- [61] M. Albooyeh, M. Hanifeh, M. Kamandi, M. Rajaei, J. Zeng, H. K. Wickramasinghe, and F. Capolino, in *2017 IEEE International Symposium on Antennas and Propagation & USNC/URSI National Radio Science Meeting* (IEEE, New York, 2017), pp. 35–36.
- [62] L. V. Poulikakos, J. A. Dionne, and A. García-Etxarri, *Symmetry* **11**, 1113 (2019).
- [63] G. Nienhuis, *Phys. Rev. A* **93**, 023840 (2016).
- [64] J. Lekner, *J. Opt.* **21**, 035402 (2019).
- [65] D. M. Lipkin, *J. Math. Phys.* **5**, 696 (1964).
- [66] A. E. Krasnok, A. E. Miroshnichenko, P. A. Belov, and Y. S. Kivshar, *Opt. Express* **20**, 20599 (2012).
- [67] D. Permyakov, I. Sinev, D. Markovich, P. Ginzburg, A. Samusev, P. Belov, V. Valuckas, A. I. Kuznetsov, B. S. Luk'yanchuk, A. E. Miroshnichenko, D. N. Neshev, and Y. S. Kivshar, *Appl. Phys. Lett.* **106**, 171110 (2015).
- [68] A. I. Kuznetsov, A. E. Miroshnichenko, M. L. Brongersma, Y. S. Kivshar, and B. Luk'yanchuk, *Science* **354**, aag2472 (2016).
- [69] G. Boudarham, R. Abdeddaim, and N. Bonod, *Appl. Phys. Lett.* **104**, 021117 (2014).
- [70] A. García-Etxarri, R. Gómez-Medina, L. S. Froufe-Pérez, C. López, L. Chantada, F. Scheffold, J. Aizpurua, M. Nieto-Vesperinas, and J. J. Sáenz, *Opt. Express* **19**, 4815 (2011).
- [71] M. Kerker, D.-S. Wang, and C. L. Giles, *J. Opt. Soc. Am.* **73**, 765 (1983).
- [72] L. D. Landau, J. S. Bell, M. J. Kearsley, L. P. Pitaevskii, E. M. Lifshitz, and J. B. Sykes, *Electrodynamics of Continuous Media* (Elsevier, New York, 2013).
- [73] C. R. Simovski and S. A. Tretyakov, *Phys. Rev. B* **79**, 045111 (2009).
- [74] S. Campione, C. Guclu, R. Ragan, and F. Capolino, *ACS Photonics* **1**, 254 (2014).
- [75] M. Darvishzadeh-Varcheie, C. Guclu, and F. Capolino, *Phys. Rev. Appl.* **8**, 024033 (2017).
- [76] A. Alù and N. Engheta, *Opt. Express* **17**, 5723 (2009).
- [77] S. Mühlig, A. Cunningham, S. Scheeler, C. Pacholski, T. Bürgi, C. Rockstuhl, and F. Lederer, *ACS Nano* **5**, 6586 (2011).
- [78] V. Ponsinet, P. Barois, S. M. Gali, P. Richetti, J. B. Salmon, A. Vallecchi, M. Albani, A. Le Beulze, S. Gomez-Grana, E. Duguet, S. Mornet, and M. Treguer-Delapierre, *Phys. Rev. B* **92**, 220414(R) (2015).
- [79] M. Rahmani, E. Yoxall, B. Hopkins, Y. Sonnefraud, Y. Kivshar, M. Hong, C. Phillips, S. A. Maier, and A. E. Miroshnichenko, *ACS Nano* **7**, 11138 (2013).
- [80] A. Vallecchi, M. Albani, and F. Capolino, *Opt. Express* **19**, 2754 (2011).
- [81] D. Kajfez and P. Guillon, *Dielectric Resonators* (Artech House, Norwood, MA, 1986).
- [82] O. Merchiers, F. Moreno, F. González, and J. M. Saiz, *Phys. Rev. A* **76**, 043834 (2007).
- [83] I. Staude, V. V. Khardikov, N. T. Fofang, S. Liu, M. Decker, D. N. Neshev, T. S. Luk, I. Brener, and Y. S. Kivshar, *ACS Photonics* **2**, 172 (2015).
- [84] I. Sinev, I. Iorsh, A. Bogdanov, D. Permyakov, F. Komissarenko, I. Mukhin, A. Samusev, V. Valuckas, A. I. Kuznetsov, B. S. Luk'yanchuk, A. E. Miroshnichenko, and Y. S. Kivshar, *Laser Photonics Rev.* **10**, 799 (2016).
- [85] I. Staude, A. E. Miroshnichenko, M. Decker, N. T. Fofang, S. Liu, E. Gonzales, J. Dominguez, T. S. Luk, D. N. Neshev, I. Brener, and Y. Kivshar, *ACS Nano* **7**, 7824 (2013).
- [86] R. M. Bakker, D. Permyakov, Y. F. Yu, D. Markovich, R. Paniagua-Domínguez, L. Gonzaga, A. Samusev, Y. Kivshar, B. Luk'yanchuk, and A. I. Kuznetsov, *Nano Lett.* **15**, 2137 (2015).
- [87] W. Liu, A. E. Miroshnichenko, D. N. Neshev, and Y. S. Kivshar, *ACS Nano* **6**, 5489 (2012).
- [88] Y. H. Fu, A. I. Kuznetsov, A. E. Miroshnichenko, Y. F. Yu, and B. Luk'yanchuk, *Nat. Commun.* **4**, 1527 (2013).
- [89] B. S. Luk'yanchuk, N. V. Voshchinnikov, R. Paniagua-Domínguez, and A. I. Kuznetsov, *ACS Photonics* **2**, 993 (2015).
- [90] X. Zambrana-Puyalto and N. Bonod, *Nanoscale* **8**, 10441 (2016).
- [91] D. E. Aspnes and A. A. Studna, *Phys. Rev. B* **27**, 985 (1983).
- [92] C. F. Bohren and D. R. Huffman, *Absorption and Scattering of Light by Small Particles* (John Wiley & Sons, New York, 2008).
- [93] M. Darvishzadeh-Varcheie, M. Kamandi, M. Albooyeh, and F. Capolino, *Opt. Lett.* **44**, 4957 (2019).
- [94] M. Veysi, C. Guclu, and F. Capolino, *J. Opt. Soc. Am. B: Opt. Phys.* **32**, 345 (2015).